International Journal of Physical Modelling in Geotechnics
Pages 1–20

Keywords: Centrifuge modelling; Strain; Piles & piling; Retaining walls; Soil/structure interaction; Tunnels & tunnelling

ice | **proceedings**

The application of FBGs for centrifuge testing: pile axial loads and wall bending moments

Geyang Song (Orcid: 0000-0002-0832-6991)
Nottingham Centre for Geomechanics, Faculty of Engineering, University of Nottingham, Nottingham, NG7 2RD, UK.
Jingmin Xu (Orcid: 0000-0002-5814-247X)
Institute of Geotechnical Engineering, School of Transportation, Southeast University, Nanjing, 211189, China; Formerly, Faculty of Engineering, University of Nottingham, Nottingham, NG7 2RD, UK.
Charles M. Heron (Orcid: 0000-0002-7935-4703)
Nottingham Centre for Geomechanics, Faculty of Engineering, University of Nottingham, Nottingham, NG7 2RD, UK
Alec M. Marshall (Orcid: 0000-0003-1583-1619)
Nottingham Centre for Geomechanics, Faculty of Engineering, University of Nottingham, Nottingham, NG7 2RD, UK
Ricardo Correia (Orcid: 0000-0001-6405-5340)
Optics and Photonics Group, Faculty of Engineering, University of Nottingham, Nottingham, NG7 2RD, UK
Sergiy Korposh (Orcid: 0000-0001-5179-6991)
Optics and Photonics Group, Faculty of Engineering, University of Nottingham, Nottingham, NG7 2RD, UK

One challenge for geotechnical centrifuge testing of soil-structure interaction problems is the reliable measurement of induced structural strains/forces. This paper presents a novel application of fibre Bragg grating (FBG) sensors for strain measurement within geotechnical centrifuge tests. FBG sensors have several advantages for centrifuge testing, in particular their small size and minimal self-weight. This paper gives an overview of recently developed installation and calibration procedures for FBG sensors within buried centrifuge model structures. The effect of thermal expansion/contraction of the materials (including both the fibre and structures) is considered and assessed. The precision and reliability of the FBG sensors are demonstrated using verification tests. The application of the FBG sensors is considered for two geotechnical problems, namely, pile jacking and a 'retaining wall' adjacent to a tunnel (acting as a protective wall to prevent an adjacent structure from tunnelling induced ground movement). Results demonstrate that the FBG sensors can provide reliable measurements of pile axial strains/forces and protective wall bending moments. The paper provides evidence to support the routine adoption of FBG sensors for strain/force measurement of structures in geotechnical centrifuge modelling.

1. Introduction

In the context of geotechnical centrifuge testing, strains within model structures are generally measured using conventional foil strain gauges. However, conventional strain gauges have several limitations with respect to the small-scale models adopted within geotechnical centrifuge tests. For example, centrifuge models of common pile foundations are typically made from hollow tubes measuring between 9 and 12 mm (Loganathan *et al.*, 2000; Jacobsz, 2003), which prohibits or poses significant challenges for the installation of the strain gauges within the interior of the model pile. Therefore, the strain gauges are commonly bonded to the outer surface of the piles (Loganathan *et al.*, 2000; Lee and Chiang, 2007; Ng and Lu, 2013), which can affect the surface profile of the model pile or alter the intended mechanical properties. Moreover, the quality of the output signal of foil strain gauges is affected by the electromagnetic field within a geotechnical centrifuge, which could affect the performance of the tests.

Another option for measuring strain comes from the use of fibre Bragg Grating (FBG) sensors. Optical fibre sensors are immune to the effects of electromagnetic fields and are smaller and lighter than conventional foil strain gauges. FBG sensors have been used in full-scale field experiments for monitoring piles, tunnels and structures (Doherty *et al.*, 2015; Schmidt-Hattenberger *et al.*, 2003; Baldwin *et al.*, 2001; Li *et al.*, 2014; Lee *et al.*, 2004; Kister *et al.*, 2007; MacPherson *et al.*, 2006; Ye *et al.*, 2013; Majumder *et al.*, 2008). The applications of FBG sensors within geotechnical centrifuge tests are relatively limited (Beemer *et al.*, 2018; Correia *et al.*, 2016; Zhang *et al.*, 2019), though recently Li *et al.* (2020) provided a thorough demonstration of how FBG sensors can be used to measure the bending moment of a monopile subjected to horizontal loading within a geotechnical centrifuge. Li *et al.* (2020) demonstrated an example of FBG sensor installation, the calibration, and the processing of FBG data for measurement of bending moments. This paper follows a similar theme to that of Li *et al.* (2020), demonstrating recent experiences with FBG applications, but is distinct in several areas, namely the FBG installation techniques, the use of fibre optic splitters (couplers) to increase the number of FBG gauge inputs, and the measurement of axial loads (which requires consideration of temperature effects that do not affect the measurement of bending moments).

This paper is intended to give an overview of insights and lessons gained from recent experiences of researchers at the University of Nottingham Centre for Geomechanics (NCG). The paper presents detailed information about the installation and calibration of FBG sensors for the measurement of axial forces within model piles and bending moments within a buried protective wall adjacent to a tunnel. The paper provides data from two pile jacking tests and one test where a buried protective wall was used to reduce foundation/building displacements caused by tunnelling. Results from theses centrifuge tests are used to demonstrate the feasibility of using FBG sensors within geotechnical centrifuge tests.

2. Principle of FBG sensors

FBG sensors consist of an optical fiber onto which a "grating" is inscribed by using an excimer laser. This grating consists of several etches over a certain length of the fiber at a regular spacing (Λ, referred to as the "grating pitch"). When broad wavelength light is injected into the fibre, a specific narrow-band spectrum is reflected by the grating, as illustrated in Figure 1. The wavelength of the reflected light depends on the grating pitch which in turn is affected by the strain level within the fibre. Hence, by measuring the shift in the wavelength ($\Delta\lambda_B$) of the reflected light (referred to as a "Bragg"), the magnitude of strain within the fibre at the grating location can be determined. The wavelength of the reflected light is also affected by the reflective index (n) of the fiber which is dependent on the ambient temperature and pressure the fiber is subjected to (Kersey *et al.*, 1997). The reflected Bragg wavelength λ_B can be expressed as:

$$\lambda_B = 2n\Lambda \tag{1}$$

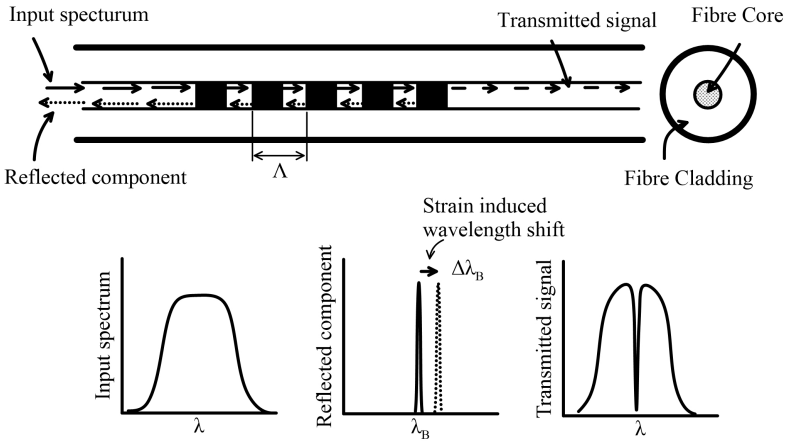

Figure 1. Basic Bragg grating process, after Kersey *et al.* (1997)

3. Instrumentation and calibration of FBG sensors

3.1. Models and instrumentation

3.1.1. Model piles

In this study, the model piles were made of hollow aluminium tubes to match the axial stiffness of concrete piles. Two pile sizes, in terms of outer diameter, are considered: 10 mm and 12 mm; both piles have a wall thickness of 1 mm. To increase the interface roughness, sands was bonded to the surface and tip of the model piles (the same sand used for the soil body) using epoxy, which gave a final pile diameter

of 11 mm and 13 mm. A consistent prototype scale pile diameter of 0.88 m was considered by adopting different centrifuge acceleration levels for the two piles; 80 g for the 11 mm pile and 68 g for the 13 mm pile. In practice, a 0.8 m diameter concrete pile has an axial stiffness $EA = 10 - 14 \times 10^3$ MN, assuming concrete has a Young's modulus E ranging from 20-28 GPa. For the 10 and 12 mm diameter model piles (ignoring the contribution of the epoxy/sand coating), the theoretical prototype scale values of axial rigidity EA are 19.4×10^3 and 13.5×10^3 MN, respectively, which are comparable to the value of the 0.8 m full-scale concrete pile. The focus of the tests was the axial loading of the piles, hence bending of the piles was not assessed.

FBG sensors were attached to the inner surface of the model piles to measure the physical strain. Therefore, the elongation strain of the FBG sensors (ε) can be directly correlated to the physical strain along the model pile (ε_t). The FBG sensors were made from a single-mode optical fibre and written by an excimer laser (reflectivity of 90%) with a centre wavelength of 1530, 1535, and 1540 nm or 1545, 1550, 1560 nm. Figure 2 illustrates the instrumentation procedures, with label numbers referred to below. The pile is first clamped into place and the fibre, which contains the FBG sensors, is placed inside the pile, with one end of the fibre covered by a small plastic tube to protect the fibre from damage during centrifuge tests. An ultraviolet (UV) cured adhesive is used to fix the fibre at the upper entry point of the model pile; label (1) in Figure 2. Superglue (Loctite Superglue precision) is then used to adhere a small length of the fibre inside the pile, as shown by label (2). Once the superglue is fully cured, the other end of the fibre is clamped to a modified micrometre terminal; label (3). By moving the modified micrometre outwards, the fibre is 'stretched' along the inner surface of the aluminium tube; label (4). Superglue is then applied along the fibre, followed by a layer of the UV cured adhesive to ensure the FBG sensors are fully attached to the aluminium pile; label (5). Data from the preliminary centrifuge tests (discussed later in this paper) suggested that the use of the UV cured adhesive is not necessary and caused over-registering of the FBG sensors.

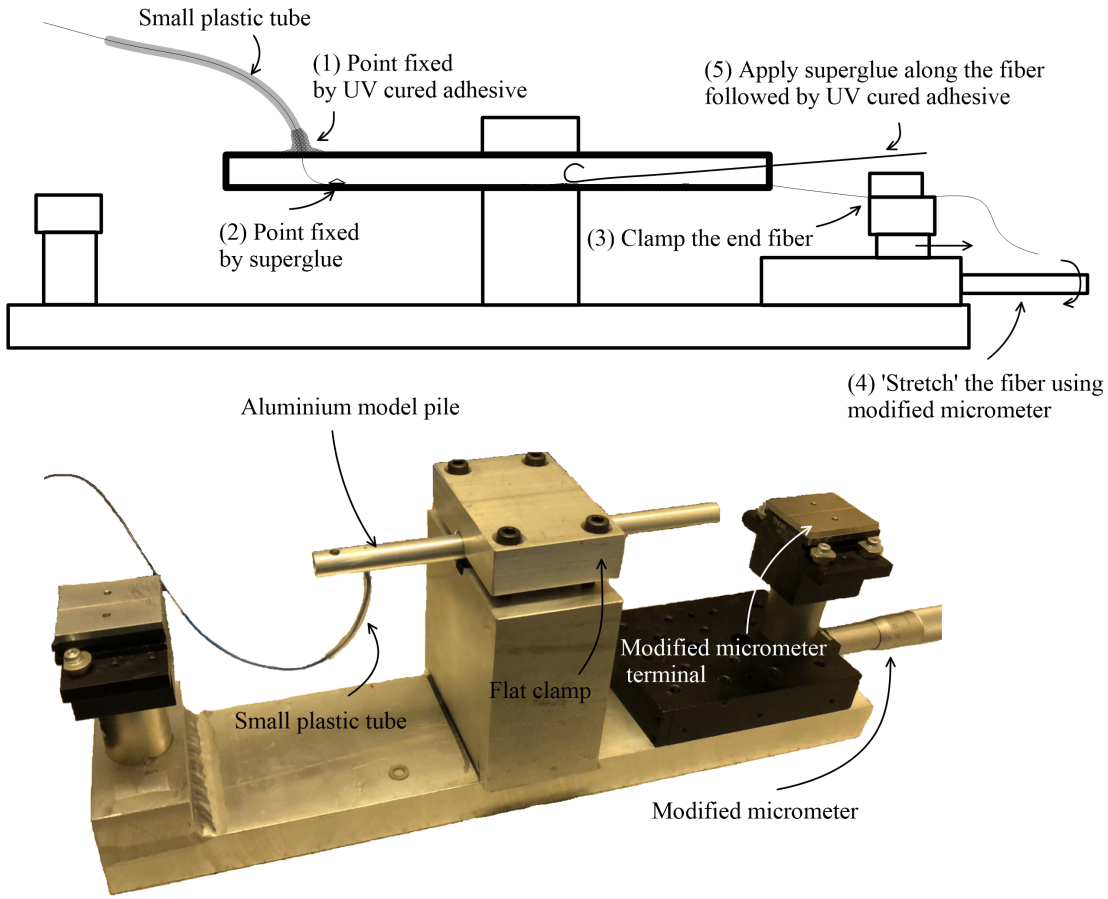

Figure 2. FBG sensor installation procedure

3.1.2. Model protective wall

A 10 mm thick aluminium plate with a width of 148 mm was used in the centrifuge test to model a protective wall adjacent to a tunnel, which gives a flexural rigidity $EI = 34.8 \times 10^3$ MNm^2 in prototype scale (80 g). Using a geometric scaling factor, the aluminium plate represents a 0.8 m thick wall at prototype scale. However, an unreinforced 0.8m thick concrete wall has a flexural rigidity of $EI = 10 - 14 \times 10^3$ MNm^2 (assuming the same range of E as used previously). Therefore, in terms of flexural rigidity, the aluminium plate represents a concrete wall that has a thickness of between 1 and 1.2 m. Sand was bonded to the surface and base of the model wall to increase the interface roughness, consistent with the method adopted for the piles.

FBG sensors were used to measure the bending moments along the protective wall during centrifuge tests. The sensors were installed on opposing sides of the wall at the middle and quarter width of the wall, as shown in Figure 3. The FBG fibre installation procedure can be summarised as follows: (1) four 1 mm deep, 1.5 mm wide slots were machined into the opposing faces of the aluminium plate. (2) Four fibres (each containing five FBG sensors) were then placed inside the four slots and covered by superglue. The UV cured adhesive was not used for the wall model because of issues relating to the effect of the adhesive's self-weight on FBG readings (a lesson learned from the preceding tests on piles), as discussed in subsection 4.3. (3) Brass U-channels were installed in the slots and secured with superglue. The depth of the slots is greater than the diameter of the fibres to provide clearance between the fibre and the brass U-channel. This setup protects the FBG sensors from the effects of the soil pressures during centrifuge tests, which would affect FBG readings.

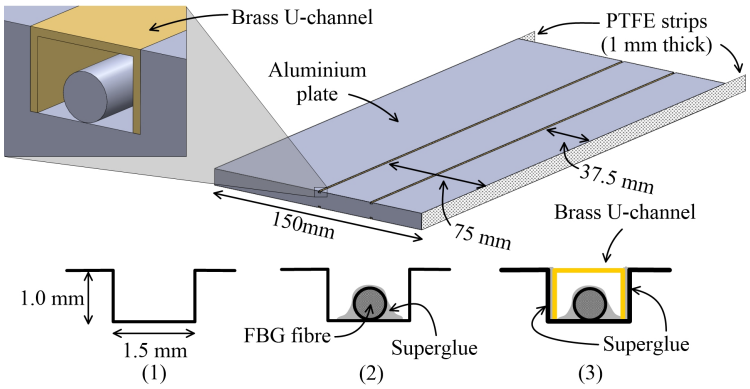

Figure 3. FBG sensor installation for model protective wall

3.2. FBG sensor calibration

Calibration tests were conducted on the model piles and protective wall to correlate the variables between mechanical strain (i.e. due to an applied load or bending) and FBG wavelength shift. The calibration tests were conducted within a temperature-controlled room such that temperature effects could be discounted.

3.2.1. Model pile axial force calibration

The strain measured from FBG sensors (ε) is not necessarily identical to the physical strain of the aluminium pile (ε_t); this is because the physical strain of the pile is transmitted to the FBG sensor through the bonding agents (superglue and UV adhesive, as described in the previous subsection). The axial force along the pile can be calculated as $F = EA\varepsilon_t$, where $\varepsilon_t \propto \varepsilon$, $\varepsilon = \Delta\lambda_B / K_\varepsilon$, and E and A are Young's modulus and cross-sectional area of the aluminium pile, respectively. As such, axial force (F) was correlated with FBG wavelength shift ($\Delta\lambda_B$) through calibration tests, as illustrated in Figure 4. A Global Digital Systems (GDS) load frame was used to apply the axial compressive force along the pile. The 11 mm diameter model piles contain 6 FBG sensors (3 on each side of the pile, denoted B1-B6 in Figure 4). The 13 mm diameter piles contain 10 FBG sensors (5 on each side of the pile). A calibrated load cell was fixed at the top of the loading frame, where an adapter was used between the calibrated load cell and pile tip to generate a uniform pressure over the pile tip.

Figure 4 (a) demonstrates the loading sequence to calibrate the FBG sensors. Both model piles were calibrated three times, with each calibration sequence consisting of twelve loading steps. The load applied during every step was held for $\approx$ 10 s. Figure 4 (b) shows the axial force applied to one of the 11 mm diameter model piles along with the measured wavelength shift of FBG sensor B4 during one of the three calibrations. A linear line is fitted to the data and the gradient K_{B_i} is obtained. The axial force along the pile for a particular FBG sensor (B$_i$) is then calculated as $F_i = K_{B_i}\Delta\lambda_{B_i} + \lambda_{OS_i}$, where the subscript i is the FBG reference number (see Figure 4) and λ_{OS_i} is

the wavelength offset. A unique value of K_{B_i} is obtained for each FBG sensor (B_i). The average value of K_{B_i} for each FBG sensor from the three calibrations was used.

For the applied axial loading, it is assumed that the axial forces applied to the two fibres at a given pile location (i.e. those on opposing sides of the pile) were identical. Therefore, the average of the readings of two FBG sensors at a given pile location are used to calculate the axial force of the pile. For the 11 mm diameter model pile, there are three axial force measurement depths, denoted S1 to S3, see Figure 7. The same principle applies to the 13 mm diameter model pile, which has five axial force measurement points.

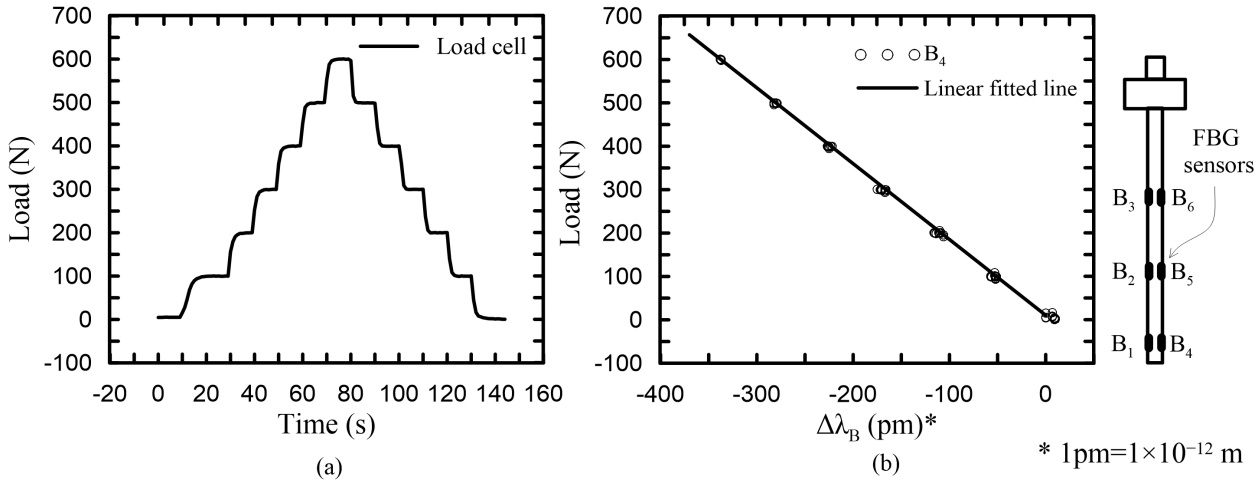

Figure 4. Model pile axial force calibration: (a) loading sequence; (b) Pile 3 B_4 result

3.2.2. Model wall bending moment calibration

Similar to the axial force calibration, the bending moment of the model protective wall at a particular FBG sensor location (M_i) was directly correlated with the FBG wavelength shift ($\Delta\lambda_B$). Figure 5 shows the bending moment calibration setup using a 3-point bending test arrangement (similar to that described by Li *et al.* (2020)). Two aluminium angles are located at specific locations at the ends of the wall and a steel rod, used to load the plate, is placed within the middle of the wall. A rubber strip is placed under the rod to ensure the load is applied evenly across the width of the model wall. Two cable ties are used to transfer the load from a mass hanger to the steel bar. The distance between the two cable ties to the centreline of the aluminium wall is identical, hence the force from the two cable ties is equal. Three loading positions were used to conduct the calibration: 90, 130 and 180 mm away from the right-side support position (see Figure 5). For each loading location, three loading cycles were conducted, with weight being added to the mass hanger in 1 kg increments up to a maximum weight of 13 kg. Once three loading locations were completed, the model wall was flipped over and the calibration procedure described above repeated (the two faces of the wall were labelled as Side S1 and S2, as shown in Figure 5). The five bending moment measurement locations (five FBG sensors) are denoted $P_1 - P_5$, as illustrated in Figure 5.

During the calibration process with the wall Side S1 facing upwards, the change in wavelength of the FBG sensors located on Side S1 ($\Delta\lambda_{B,P_{iS1}}$) is negative (under compression), and the change in wavelength of the FBG sensors on Side S2 ($\Delta\lambda_{B,P_{iS2}}$) is positive (under tension). Therefore, the change in wavelength $\Delta\lambda_{B,P_i}$ at location P_i can be taken as the difference of change in wavelength from both FBG sensors and can be expressed as $\Delta\lambda_{B,P_i} = \Delta\lambda_{B,P_{iS1}} - \Delta\lambda_{B,P_{iS2}}$, where subscript i is the FBG sensor location index ($i = 1 - 5$) and subscript S1 or S2 refers to the wall side. For bending moment sign convention, the bending moment (M_i) is taken as positive when the calibration was conducted with wall Side S1 facing upwards (see Figure 5).

Figure 6 shows the change in wavelength $\Delta\lambda_{B,P_i}$ (combination of change in wavelength from both FBG sensors) for position P_3 with applied bending moment (M_3). A linear line was fitted to the data with the gradient giving K_{B,P_i}. The bending moment for a particular FBG location (P_i) was calculated as $M_i = K_{B,P_i} \times \Delta\lambda_{B,P_i}$.

3.3. FBG temperature compensation

The wavelength shift of the FBG sensors caused by physical elongation (strain ε) was obtained by the calibration procedures described in the previous subsection. Pressure compensation is not required since the FBG sensors were not in direct contact with the soil during

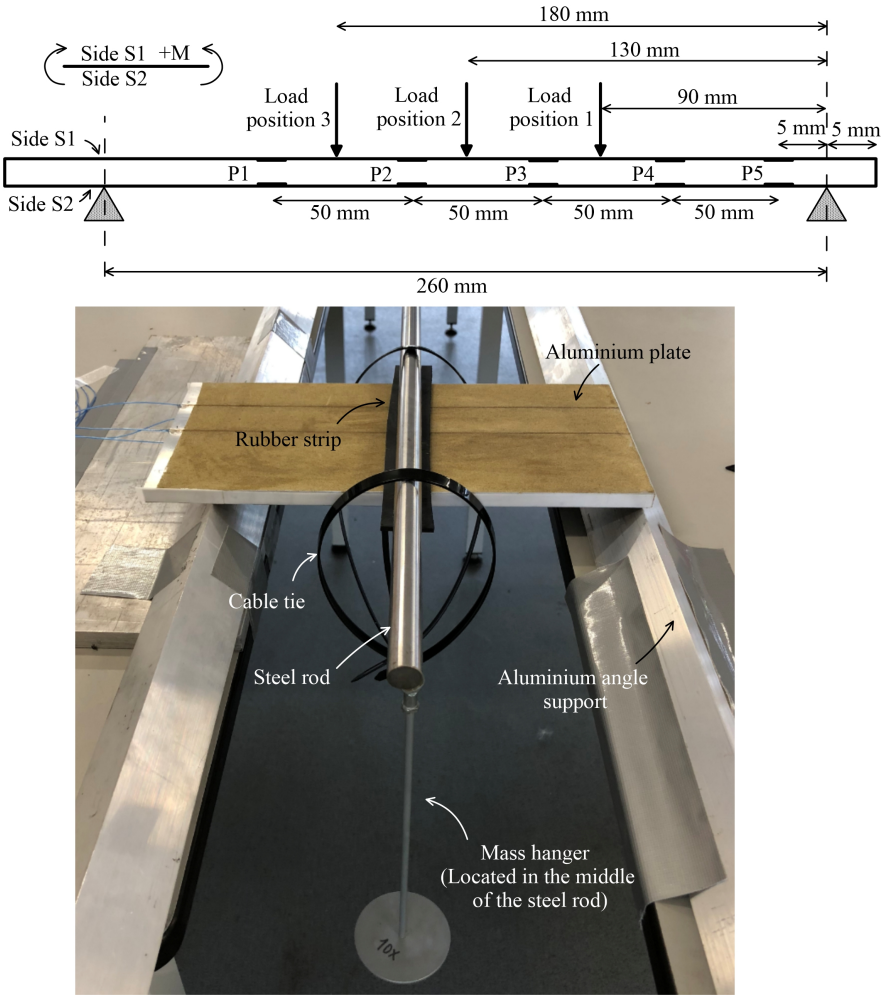

Figure 5. Bending moment calibration for FBG sensors

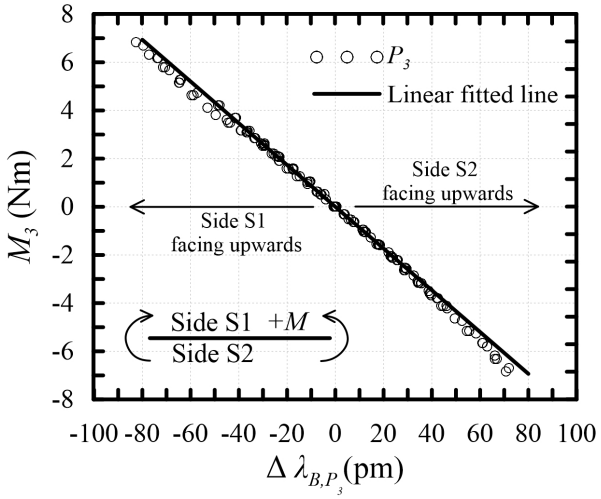

Figure 6. Change in wavelength at location P_3 ($\Delta\lambda_{B,P_3}$) with bending moment (M_3)

centrifuge tests. Thermal expansion/contraction of the aluminium and fibre will cause additional elongation strain, which will affect the FBG wavelength shift, therefore temperature compensation is required.

For the protective wall, since bending moments are calculated as the differences in FBG wavelength shift on both sides of the wall ($\Delta\lambda_{B,P_i} = \Delta\lambda_{B,P_{iS1}} - \Delta\lambda_{B,P_{iS2}}$) and the temperature effects will be identical for these FBG sensors, the temperature effect is self-compensated and no corrections are required (which was also the case for Li *et al.* (2020)).

For the model piles, to obtain the relationship between change in model pile temperature change (ΔT_p) and FBG wavelength shift due to this temperature ($\Delta\lambda_{B_it}$), a 'dummy' pile (made from the same aluminium tube as the 13 mm model pile) instrumented with temperature sensors (thermocouples) was used. The instrumented piles with FBG sensors were placed inside a temperature controlled chamber, along with the dummy pile. Note that the temperature given by the chamber is not necessarily the temperature experienced by the model pile. Therefore, a dummy pile is used to measure the temperature of the model pile, with the assumption that the model pile temperature is identical to the dummy pile. Temperature sensors from the dummy pile (measuring change in pile temperature ΔT_p) and FBG sensors ($\Delta\lambda_{B_it}$) were connected to a National Instruments Data Acquisition (DAQ) system and FBG interrogator, respectively.

The piles were calibrated for temperatures ranging between 20-25°C, corresponding approximately to the variation of the centrifuge chamber temperature (ΔT) during tests, providing a linear relationship between change in pile temperature (ΔT_p) and FBG wavelength shift ($\Delta\lambda_{B_it}$). In a centrifuge test, the dummy pile was buried within the soil, similar to the FBG instrumented piles, providing a measurement of pile temperature throughout the test. Using the measured dummy pile temperature and the obtained temperature calibration factors, the FBG readings from the piles were corrected for the effect of temperature change.

3.4. FBG system setup

The FBG system setup is demonstrated in Figure 7 for a centrifuge test involving four 11 mm diameter instrumented model piles. To reduce the number of signals from the eight fibres (each of the four piles contain two fibres) down to four for the FBG interrogator, fibre optic splitters (couplers) were used, which gives an even split ratio from one input fibre (regardless of input wavelength) to two output fibres; a detailed configuration is shown in Figure 7. Data is transferred via ethernet cable from the FBG interrogator to an on-board gigabit switch (labelled as switch (1) in Figure 7). The FBG interrogator and gigabit switch (1) are mounted in the centrifuge data acquisition system (DAS) cabinet and exposed to g-levels of 4-7 g during the centrifuge tests (80 g). The Gigabit switch (1) is connected to a fibre optic rotary joint via a subscriber connector (SC) optical cable, and the output from the rotary joint is received by Gigabit switch (2) in the centrifuge control room and linked to a control PC.

4. Preliminary centrifuge tests with model piles

To verify the FBG instrumented model pile performance in the centrifuge, a preliminary test was conducted on the NCG 2 m radius, 50 g-tonne geotechnical centrifuge. The test investigated the reliability of FBG sensor readings during centrifuge spin up (Test SU), which required the piles to be loaded axially under elevated gravity; no soil was used in the test.

4.1. Pile loading system

The pile loading system is presented in Figure 8 and allows individual load or displacement control (via LabVIEW) of each model pile. The modular actuator system allows for easy adaptation of specific test configurations. Each model pile is connected to an actuator via a loading shaft with a 5 kN in-line load cell. A die spring (stiffness rate of 219 N/mm) is required between the driving actuator and pile loading shaft to reduce the sensitivity of the load response to movements of the actuator, which was necessary to ensure the control system remained stable (Franza and Marshall, 2018b). LVDTs are located at the base of the supporting frame with their armatures resting on a plate fixed to the pile head. The linear actuators have a maximum stroke of 40 mm with a 3 kN axial load capacity.

4.2. Testing procedure

Four FBG instrumented 11 mm diameter model piles were placed inside the centrifuge strong box, with the pile tip resting on a solid wooden block (no soil or model tunnel were included; see Figure 9). A 5 N constant load was applied to the pile head via the loading system. The centrifuge was then spun to the designated speed, achieving 80 g at a point one-third the height of the centrifuge strongbox from its base.

4.3. Results

At 80 g, the total amount of force at the pile tip due to the self-weight of all components (i.e. pile, pile cap, LVDT armature and plate) and the applied 5 N pile head load is around 86 N, as shown in Figure 9 by the 'Pile self-weight' line, which shows the theoretical variation of pile load based on pile self-weight and the variation of g-level (the g-level at the 'top' (where the ground surface exists in later tests) and

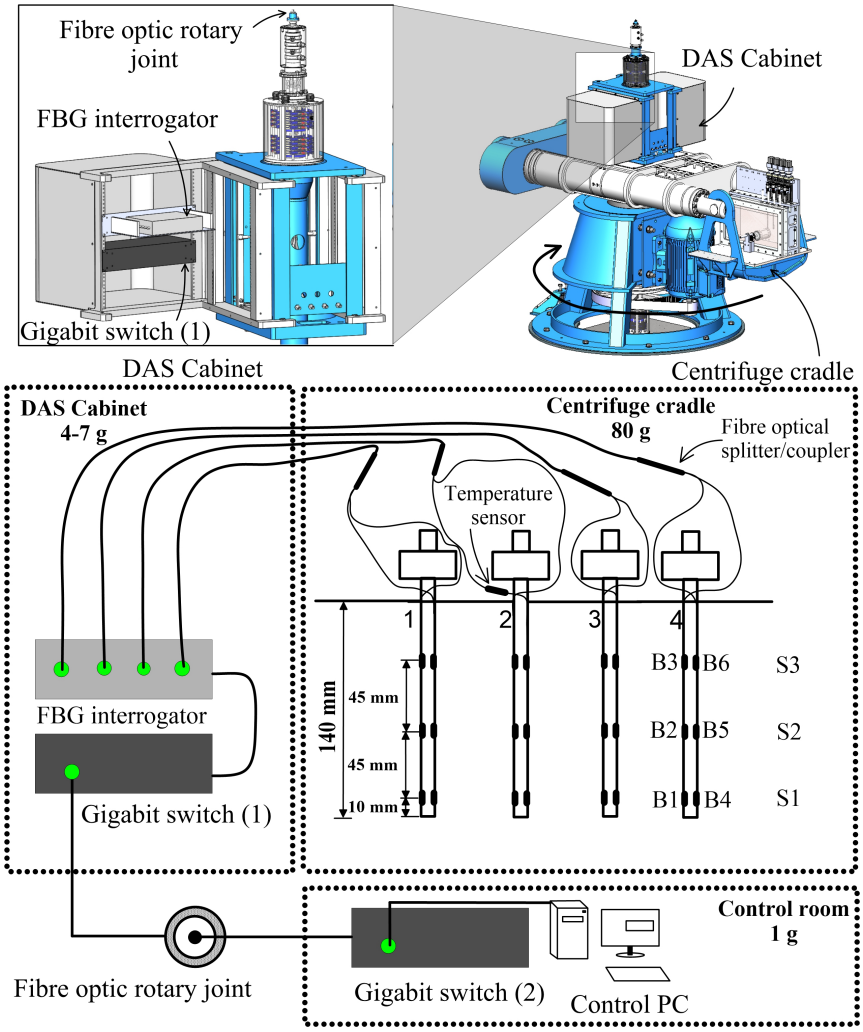

Figure 7. Schematic diagram of FBG sensor system within the centrifuge (after Song and Marshall (2020b))

tip of the piles is also provided). Figure 9 also shows the FBG sensor readings after reaching the designated centrifuge acceleration (i.e. nominally 80 g for this test).

The FBG sensors should provide force measurements that match the theoretical profile due to pile self-weight; the data in Figure 9 shows that this is not the case, with FBG sensors generally over-registering the theoretical values. Piles 2, 3, and 4 over predict the axial force along the pile, whereas pile 3 under predicts axial force within the middle and lower portions of the pile. As mentioned earlier, the FBG sensors were bonded to the piles using superglue and an additional coating of UV cured adhesive. It is believed that the UV cured adhesive, in particular, was 'over-applied' at some locations and, due to its increased self-weight during centrifuge acceleration, caused additional compressive (over predict) or extension (under predict) strain at some FBG sensor locations. These over or under predictions depend on the location of the FBG and 'over-applied' UV curved adhesive locations, and how close they are. This represents a lesson learned; future FBG applications (e.g. the protective walls) applied a minimal amount of adhesive (Superglue only without any UV cured adhesive) to minimise this issue. For this test, the maximum difference between measured and theoretical axial force is $\approx$ 20 N. This difference, or error, is considered acceptable within the context of the pile vertical loading tests presented here where the applied/induced loads are much higher; for example, in the pile jacking test in loose sand reported later, for the pile head load of 400 N, this corresponds to an error of 20/400=5%. In addition, this is an evaluation of the ability of the sensors to provide an accurate measurement of the absolute force along the pile during centrifuge spin-up; the accuracy of the sensors in measuring changes in forces along the pile at a given g-level (which is the more common case) is much better, as demonstrated by the results of the calibration tests presented earlier.

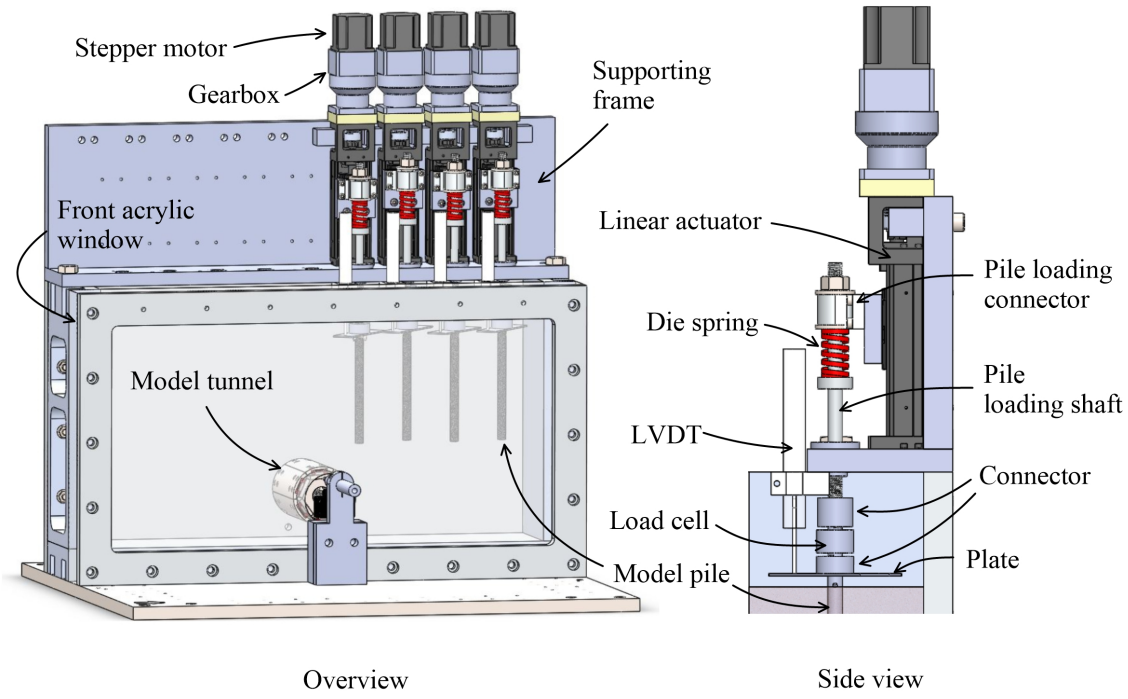

Figure 8. Pile loading system layout (after Song and Marshall (2020b))

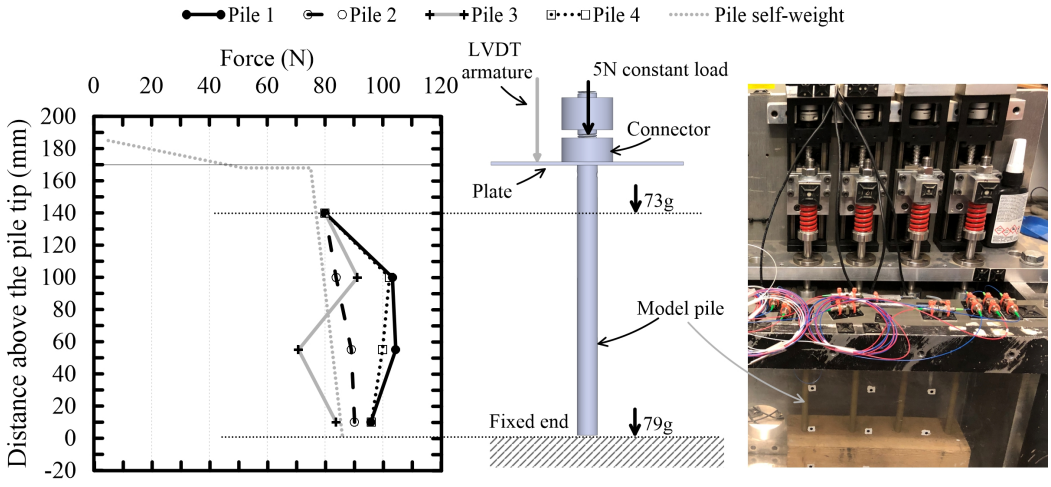

Figure 9. Test SU to verify FBG sensors under centrifuge environment

5. Application 1: pile jacking tests

5.1. Introduction

This section provides an illustration of the FBG sensor data obtained from centrifuge tests of pile jacking. Figure 10 shows the layout of the testing geometry for two pile jacking tests, referred to as PJ1 and PJ2. Note that the data from test PJ1 was also presented in Song and Marshall (2020b), where it was used within a study on the effect of tunnelling on the load redistribution of nearby piles connected to a framed building (applying the hybrid centrifuge-numerical testing approach from Idinyang *et al.* (2018); Franza and Marshall (2018a)).

There are several notable differences between the two pile jacking tests, namely: (1) Test PJ1 was conducted with 11 mm diameter piles at 80 g with a sand relative density of $I_d = 90\%$, whereas test PJ2 used a single 13 mm diameter pile at 68 g with the same sand but at a relative density of $I_d = 30\%$; (2) Test PJ1 only involved piles and soil, whereas for test PJ2, a flexible membrane (FM) model tunnel (developed by Zhou *et al.* (2014)) was located beneath the pile (30 mm separated the pile tip from the tunnel crown); (3) test PJ1 had a rigid connection between pile loading shafts and the load cells, whereas in test PJ2, the pile was not rigidly connected to the loading shaft (only downwards load could be applied).

To compensate for temperature in test PJ1, readings from an additional FBG sensor located outside pile 2 and not attached to the model piles (i.e. responding only to the ambient temperature in the centrifuge) were used. In test PJ2, the dummy pile described earlier was pre-installed in the soil at 1 g to measure temperature change within the soil during the test. Temperature sensor T4 was located above the soil surface, whereas sensors T1-3 were buried, see Figure 10.

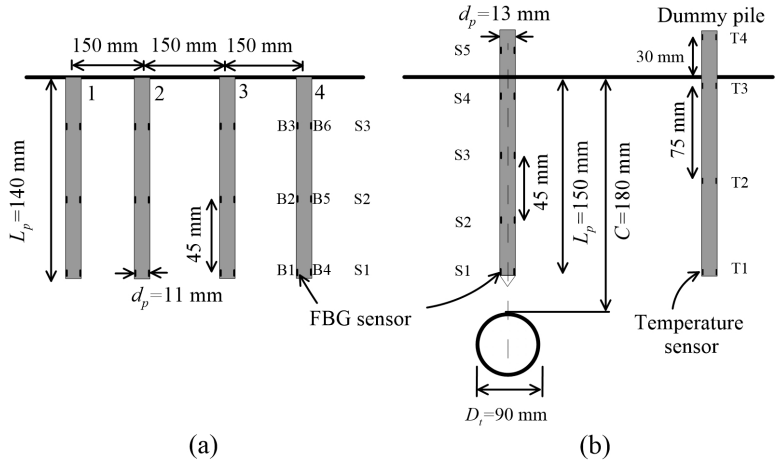

Figure 10. Test layout in model scale: (a) PJ1 (after Song and Marshall (2020b)), and (b) PJ2

5.2. Soil model and preparation

Fine-grained silica sand commonly known as Leighton Buzzard Fraction E was used for the tests; Table 1 summarises the properties of the soil. For the dense soil used in test PJ1, the sample was prepared by dry sand pouring. The strongbox was placed with the back wall facing downwards with a temporary plate used to support the sand along the plane corresponding to the ground surface, consistent with Zhou *et al.* 2014; Franza 2016. The sand was prepared according to a methodology calibrated to achieve a relative density (I_d) of 90%. The front acrylic window was then bolted to the strongbox, which was then rotated to its upright position and the temporary plate was removed, revealing the ground surface. For the loose soil sample adopted in Test PJ2, the sand was manually poured into the container to achieve a loose soil sample with a relative density I_d of approximately 30%. The repeatability of the loose sand preparation was demonstrated by Franza and Marshall (2018b) and Xu *et al.* (2020).

Table 1. Properties of the Leighton Buzzard Fraction E sand

Parameter	Value
Average diameter D_{50}	0.14 mm
Specific gravity G_s	2.65
Maximum void ratio e_{max}	1.01
Minimum void ratio e_{min}	0.61
Coefficient of uniformity C_u	1.58

To replicate non-displacement piles, the piles were pushed into the sand at 1 g. A support frame was used to ensure the piles were pushed vertically, which was temporarily connected to the strongbox side wall.

5.3. Testing procedures

In Test PJ1, a constant 5 N vertical load (model scale) was maintained at the pile head (load controlled) during centrifuge spin-up to 80 g. This was done to ensure minimum relative displacement occurred between the soil and pile during centrifuge spin-up (if fixed in place during spin-up, the soil would settle more than the pile). For Test PJ2, due to the actuator-pile connection (non-rigid; allowing pushing only), the pile head was free so that the pile could settle more than the soil during spin-up. Three stabilisation cycles (going from 68/80 g to 10 g and back to 68/80 g) were performed to encourage a uniform stress distribution within the soil body and to improve repeatability between tests.

For test PJ1, after the stabilisation cycles, the piles were jacked into the soil with an actuator jacking speed of 0.1 mm/s (due to the spring used within the actuators, the pile jacking speed varied somewhat; this would not affect results for these tests in dry sand). Once the pile settlement was greater than 20% of the pile diameter (d_p), the pile jacking was terminated. The piles were jacked in the order 2-4-1-3 (see Figure 10 for pile numbering). To reduce the pile-pile interaction effect during pile jacking, the pile spacing in test PJ1 was 150mm. For test PJ2, after centrifuge stabilisation cycles, the pile was jacked into the soil at a speed of 0.02 mm/s (the die spring was removed in this test) until a pile settlement of over 20% d_p was reached.

5.4. Test results

5.4.1. Effect of temperature change

As discussed previously, some FBG sensors over- or under-registered axial forces along the piles during centrifuge spin-up. Note that this error (offset) does not affect FBG sensor measurements during the subsequent centrifuge test at the target g-level. For example, the development of shaft resistance (the difference between two FBG measurement depths during pile jacking) is not affected by this offset. Regarding temperature effects, although the variation (in terms of pile axial force) was less than the spin-up effect (presented in the coming paragraphs), temperature variations can affect FBG readings during pile jacking; see subsection 5.4.2 for example. Therefore, it is necessary to investigate the effect of temperature change on measured results.

Figure 11 shows the recorded change in pile temperature (ΔT_p) during pile jacking for tests PJ1 and PJ2. Note that the duration of the two pile jacking tests is different. For test PJ2, all sensors show a monotonic increase in temperature with time. As expected, sensor T4 in test PJ2, located above the soil surface, shows the highest temperature readings, with readings decreasing with soil depth. For test PJ1, the change in temperature along the pile was not measured, but the additional FBG sensor located outside pile 2 provided a measurement of the ambient temperature within the centrifuge chamber.

The change in centrifuge chamber temperature (i.e. ambient air temperature) during pile jacking for tests PJ2 and PJ1 (shown on Figure 11) was about 0.4°C and 0.7°C, respectively; the difference being due to the different test duration (ambient temperature increase, caused by the centrifuge motor, over the first 10 minutes is seen to be reasonably consistent between the two tests).

Knowing that the change in temperature along the pile is less than the ambient air temperature in the centrifuge chamber (as illustrated in Figure 11 for test PJ2), a temperature change of about 0.3°C can be estimated within the pile for test PJ1 during pile jacking. Based on this temperature change, and a coefficient of thermal expansion for aluminium of $23.6 \times 10^{-6}/°\text{C}$, a variation in axial force of 12 N for the duration of the pile jacking test in PJ1 is obtained. For test PJ1, this estimated force due to temperature change was discounted from readings presented later in the paper. For results from test PJ2 (presented later), the temperature profiles obtained from the dummy pile were used to correct load readings.

5.4.2. Pile jacking

Figure 12 (a) shows the pile jacking result for test PJ2, where both load cell and FBG (S5) data versus normalised pile settlement (S_p/d_p) are presented. Note that the load cell is located above S5, which is also above the ground surface (see Figure 10). The total weight of the components between the load cell and FBG S5 (pile self-weight, connector, LVDT armature and plate) is around 186 grams, equivalent to approximately 105 N for the 57.3 g acceleration acting at the position of sensor S5 (variation of g level is considered). This force difference was used to give the 'corrected S5' line in Figure 12 (a). The difference in load reading between the load cell and the corrected S5 sensor during pile jacking is shown in Figure 12 (b). With the increase in pile settlement (S_p), the difference varied from about -10 to +15 N. This level of agreement between the two load measurement devices was seen to be satisfactory, supporting the reliability of the FBG strain sensors.

The FBG sensors provide data to evaluate the development of pile shaft average shear stress (τ_{av}) during pile jacking. The pile shaft average shear stress is calculated as the difference in axial force between two subsequent FBG measurement points. The mid-point between two

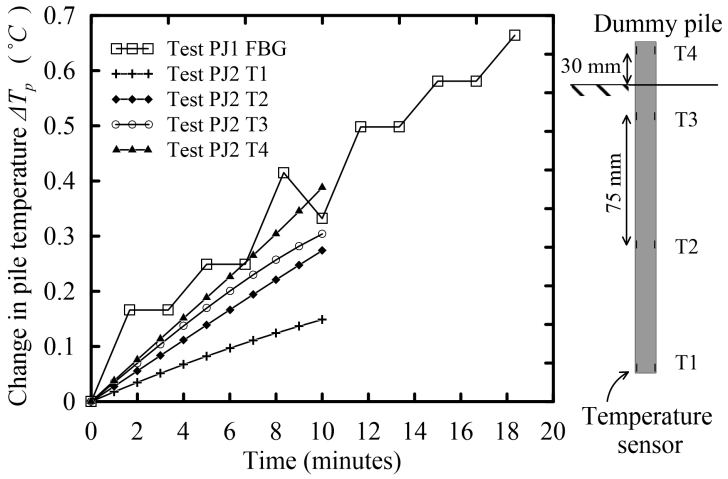

Figure 11. Change in pile temperature ΔT_p during pile jacking for tests PJ1 and PJ2

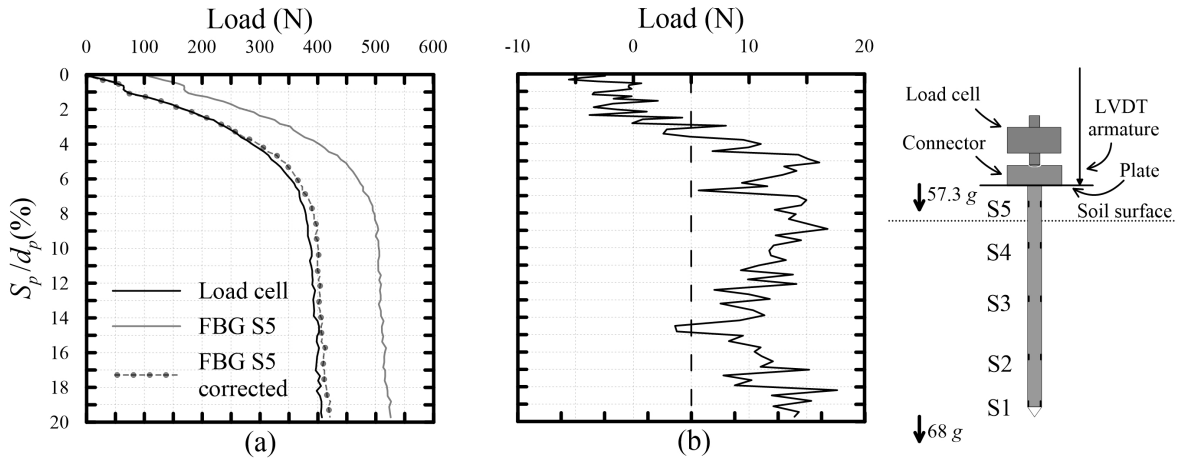

Figure 12. Test PJ2: (a) Load versus settlement and (b) difference between load cell and 'corrected' S5

FBG measurement points is used to denote soil horizons (h/R), where h is the distance between the pile tip and the specific soil horizon and R is the radius of the model pile (soil horizons illustrated in Figure 13).

Figure 13 shows the average shear stress (τ_{av}) for various soil horizons (h/R) versus normalised pile settlement (S_p/d_p) for pile 2 in test PJ1 and the pile in test PJ2. Note that, during centrifuge spin-up, uneven settlement between the pile and the surrounding soil mobilised some shaft resistance along the piles. Therefore, the initial shear stress prior to pile jacking is not zero; detailed spin-up effects on pile shaft resistance are discussed in Song and Marshall (2020b). Both piles show an increase in average shear stress with pile jacking. The shear stress magnitude in test PJ1 is always greater than in test PJ2 due to the higher soil relative density in test PJ1 ($I_d = 90\%$) compared to test PJ2 ($I_d \approx 30\%$).

The results for pile 2 in test PJ1 in Figure 13 are as expected, with the deepest soil horizon ($h/R = 5.9$) showing the largest increase of τ_{av} due to the higher effective confining stresses. After $S_p/d_p \approx 8\%$, the average shear stresses for all three soil horizons tend towards a steady-state value.

For the pile in test PJ2, the deepest soil horizon ($h/R = 3.5$) shows only a small increase of shear stress with pile jacking when compared with the shallower soil horizons ($h/R = 10.4$ and 17.3); this unexpected behaviour can be explained by the existence of the flexible

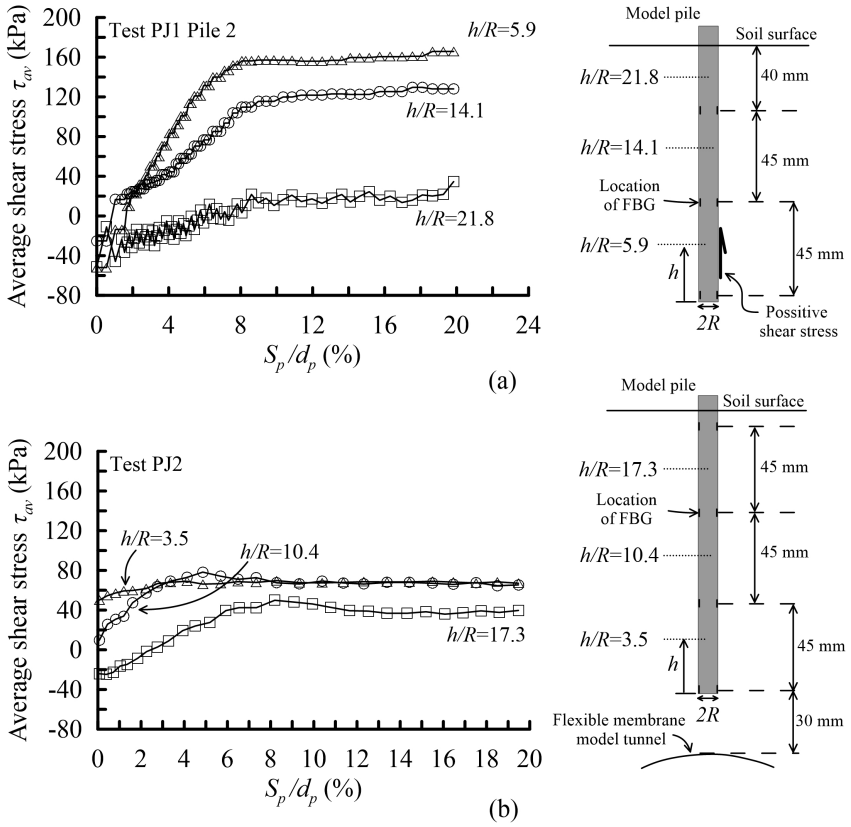

Figure 13. Average shear stress (τ_{av}) versus normalised pile settlement (S_p/d_p) for (a) test PJ1 after Song and Marshall (2020b) and (b) test PJ2

membrane model tunnel located beneath the pile tip. The FBG sensor data provided valuable insight on the effect of the model tunnel on the initial conditions of piles during pile-tunnel interaction tests, allowing better interpretation of centrifuge test results.

6. Application 2: protective wall

6.1. Introduction

This section illustrates the FBG sensor data obtained from the protective wall centrifuge test described previously. The test was part of a study on the effectiveness of protective walls to reduce tunnelling-induced settlements and distortions on nearby structures. The specific test described in this paper included a model tunnel, an FBG instrumented protective wall, four piles (instrumented with FBG sensors; See section section 3.1.1) and considered the effect of an attached steel frame structure founded on the four piles (the effect of the structure on pile loading was considered using the Coupled Centrifuge-Numerical Modelling (CCNM) approach incorporating a finite element model of the steel frame using ABAQUS; see Idinyang *et al.* (2018); Franza and Marshall (2018a)). Figure 14 shows the layout of the test, along with the definition and detail of various geometric and material parameters. This paper focuses on the bending moment data of the protective wall that was obtained from the FBG sensors. Axial loads in the piles were also obtained from the FBG sensors, however these data are not presented here due to space limitations.

6.2. Experimental set up

The centrifuge strong box has inner width × height dimensions of 700 mm × 500 mm, with a depth of 150 mm, and the 'front' face is equipped with a transparent acrylic wall. Tunnel volume loss was implemented using a 90 mm diameter eccentric rigid boundary mechanical model tunnel which enables non-uniform radial displacements around the tunnel lining (typical for shallow tunnelling), with maximum soil displacement at the tunnel crown and no displacement at the tunnel invert (Song *et al.*, 2018; Song and Marshall, 2020a). Two cameras were used to take images during the tests, and geoPIV-RG (Stanier *et al.*, 2015) was used to track subsurface soil and protective wall movements.

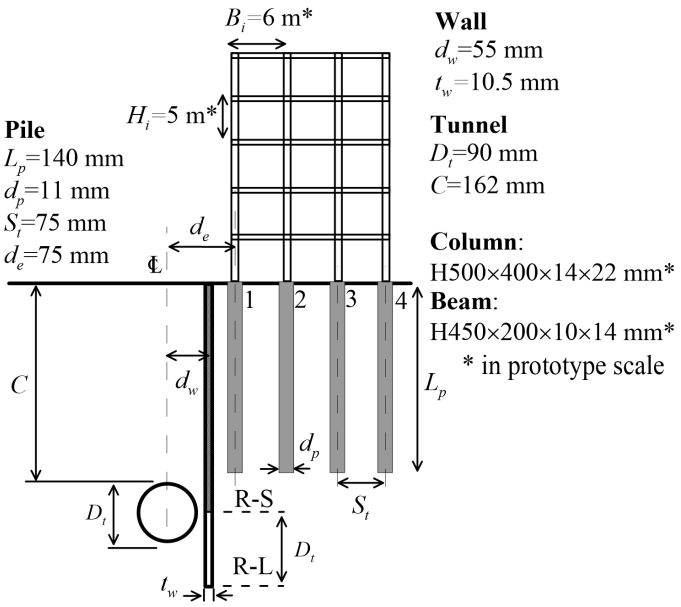

Figure 14. Experimental layout of the protective wall test

The soil sample was prepared according to the method described in the Section 5.2 (similar to pile jacking test PJ1). Prior to sand pouring, the aluminium plate (protective wall) was placed on the front acrylic window and two temporary supports were located inside the strong box to contain the sand during sand pouring. After sand pouring, the model piles were pushed into the sand sequentially, starting from pile 1 and proceeding to pile 4 (refer to Figure 14 for pile numbering); a support frame was used to ensure the piles were kept vertical during installation (see Section 5.2 for details).

6.3. Testing procedure

During centrifuge spin-up, a constant 5 N load was applied to the piles, followed by three stabilisation cycles (similar to pile jacking test PJ1). After centrifuge spin-up, the piles were then loaded to a designated working load (225 N for outer piles 1 and 4, and 370 N for inner piles 2 and 3) in 50 N stages, starting from pile 1 and moving sequentially to pile 4 (refer to pile numbering in Figure 14). The CCNM real-time data exchange interface program was then activated, followed by the initiation of ABAQUS (simulating the frame structure). The tunnel volume loss ($V_{l,t}$) process was then started, with $V_{l,t}$ increased up to $\approx 3\%$ in increments of $\approx 0.1\%$. Within the CCNM program, for each tunnel volume loss increment, pile displacements measured from the centrifuge domain are passed to the ABAQUS model via the real-time data interface, and new pile head loads calculated from ABAQUS are then passed back to the pile load control system in the centrifuge. Once a stable condition is achieved, another increment of tunnel volume loss is initiated and the process is repeated. Meanwhile, images were taken by the cameras to measure the soil and protective wall displacements.

6.4. Results

Figure 15 shows the horizontal displacement (S_h) and bending moment (obtained from the FBG sensors at the middle width of the wall) along the protective wall (depth z normalised by tunnel axis depth z_t) for a tunnel volume loss of $V_{l,t}$= 1, 2, and 3%. Note that the FBG sensors located at the quarter with of the wall presented similar results to the sensors at the middle width of the wall. Some sand intrusion between the protective wall and the acrylic window near the toe of the wall made the geoPIV-RG displacement data unreliable, hence displacements were estimated near the toe.

As a means of checking the reliability of the FBG bending moment data, finite element analyses (FEA) of the protective wall were conducted where the wall displacements from the centrifuge test (shown in Figure 15 (a)) were used to define the deformed shape of the wall. The FEA then provided a measure of the bending moments within the wall that could be compared against the FBG sensor results.

The bending moment results from the FBG sensors are compared against the FEA bending moment results in Figure 15 (b). In general, the bending moments obtained from the deformed shape of the wall (FEA) are slightly higher than the centrifuge tests, though the shape

of the bending moment profiles are similar, with maximum moments located at the lower portion of the wall (between $z/z_t = 0.6 - 0.8$, depending of $V_{l,t}$).

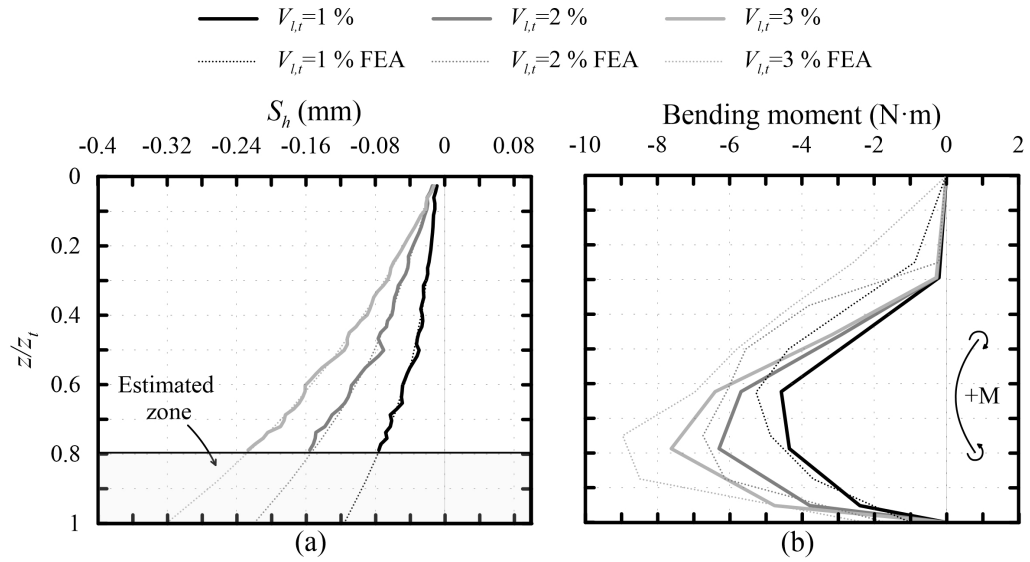

Figure 15. Horizontal displacement and bending moment along the wall with tunnel volume loss: (a) horizontal displacement, (b) bending moment

7. Conclusions

This paper demonstrated the application of FBG strain sensors within geotechnical centrifuge tests. Details were provided of FBG instrumentation installation procedures, FBG calibration, as well as temperature compensation measures. Results from a preliminary test involving piles with no soil (examining centrifuge acceleration effects on FBG measurements), two pile jacking tests, and a tunnel-protective wall-building interaction test were presented and discussed.

Compared to conventional foil strain gauges, FBG sensors are relatively light-weight, small, and can be readily attached inside small model structures, away from the effects of soil pressures and avoiding unwanted variations to the soil-structure interface.

Temperature changes, causing thermal expansion/contraction of the model structure and FBG fibres, results in FBG wavelength shifts; these effects were quantitatively assessed in this paper by measuring the FBG wavelength shift for imposed temperature changes. Results demonstrated that temperature compensation should be considered to get accurate measurements of pile axial forces (not required for measurement of bending moments); a ‘dummy’ pile embedded within the soil and instrumented with temperature sensors can provide sufficient data to allow for this compensation.

Pile axial forces measured during centrifuge spin up (with no soil included) indicated that FBG sensors were affected by the self-weight of the epoxy used to bond the optical cables, with and approximate “error” of 20 N compared to theoretical values. This “error” was not significant within the presented analysis, however it could be avoided in future projects by limiting the amount of epoxy used when bonding the FBG cables.

Splitters were used to reduce the number of FBG signals going to the interrogator; the splitter provides an even split ratio and provided stable readings during centrifuge tests. Comparison of pile force measurements from a load cell and an FBG sensor also confirmed the reliability of the FBG sensor readings, with measurements disagreeing by a maximum of 10 N. In addition, the bending moments within a protective wall subjected to tunnelling induced displacements were measured using FBG sensors. Good agreement was found between the FBG measurements of bending moments and those obtained from an evaluation of wall bending moments based on the measured deformed shape of the wall.

It was demonstrated that the FBG sensors can, with appropriate installation, calibration, and temperature correction procedures, provide reliable measurements of strains/forces and bending moments within model structures for geotechnical centrifuge testing.

NOTATION

C_u	coefficient of uniformity
d_p	pile diameter
D_{50}	average diameter of sand particle
e_{max}	maximum void ratio
e_{min}	minimum void ratio
EA	axial stiffness
EI	flexural rigidity
F_i	the axial force along the pile, where the subscript i is the FBG reference number
G_s	specific gravity
h	the distance between the pile tip and a given specific soil horizon
I_d	sand relative density
K_{B_i}	the gradient of the fitted linear line to the load calibration data, where the subscript i is the FBG reference number
K_ε	the coefficients of the wavelength sensitivity to strain (ε)
M_i	the bending moment of the model protective wall at a particular FBG sensor location, where the subscript i is the FBG reference number
n	the reflective index
R	the radius of the model pile
S_h	horizontal displacement along the protective wall
S_p	pile settlement
$V_{l,t}$	tunnel volume loss
z	depth of interest
z_t	tunnel axis depth
ΔT_p	model pile temperature change
$\Delta\lambda_{B_i}$	the shift in the wavelength, where the subscript i is the FBG reference number
λ_B	Bragg wavelength
λ_{OS_i}	the wavelength offset, where the subscript i is the FBG reference number
τ_{av}	pile shaft average shear stress
ε	the elongation strain of the FBG sensors
ε_t	the physical strain along the model pile

REFERENCES

Baldwin CS, Poloso T, Chen PC, Niemczuk JB, Kiddy JS and Ealy C (2001) Structural monitoring of composite marine piles using fiber optic sensors. In *Smart Structures and Materials 2001: Smart Systems for Bridges, Structures, and Highways*, vol. 4330, International Society for Optics and Photonics, pp. 487–498.

Beemer R, Cassidy M and Gaudin C (2018) Investigation of an ofdr fibre bragg system for use in geotechnical scale modelling. In *9th International Conference of Physical Modelling in Geotechnics: ICPMG*, pp. 279–284.

Correia R, James S, Marshall A, Heron C and Korposh S (2016) Interrogation of fibre bragg gratings through a fibre optic rotary joint on a geotechnical centrifuge. In *Proc. SPIE 9916, Sixth European Workshop on Optical Fibre Sensors*, pp. 1–4.

Doherty P, Igoe D, Murphy G, Gavin K, Preston J, McAvoy C, Byrne B, Mcadam R, Burd H, Houlsby G *et al.* (2015) Field validation of fibre bragg grating sensors for measuring strain on driven steel piles. *Géotechnique* .

Franza A (2016) *Tunnelling and its effects on piles and piled structures*. PhD thesis, University of Nottingham.

Franza A and Marshall AM (2018a) Centrifuge and real-time hybrid testing of tunneling beneath piles and piled buildings. *Journal of Geotechnical and Geoenvironmental Engineering* **145(3)**: 04018110.

Franza A and Marshall AM (2018b) Centrifuge modelling study of the response of piled structures to tunnelling. *ASCE Journal of Geotechnical and Geoenvironmental Engineering* **144(2)**: 04017109.

Idinyang S, Franza A, Heron C and Marshall AM (2018) Real-time data coupling for hybrid testing in a geotechnical centrifuge. *International Journal of Physical Modelling in Geotechnics* : 1–13.

Jacobsz SW (2003) *The effects of tunnelling on piled foundations*. PhD thesis, University of Cambridge.

Kersey AD, Davis MA, Patrick HJ, LeBlanc M, Koo K, Askins C, Putnam M and Friebele EJ (1997) Fiber grating sensors. *Journal of lightwave technology* **15(8)**: 1442–1463.

Kister G, Winter D, Gebremichael Y, Leighton J, Badcock R, Tester P, Krishnamurthy S, Boyle W, Grattan K and Fernando G (2007) Methodology and integrity monitoring of foundation concrete piles using bragg grating optical fibre sensors. *Engineering Structures* **29(9)**: 2048–2055.

Lee CJ and Chiang KH (2007) Responses of single piles to tunneling-induced soil movements in sandy ground. *Canadian Geotechnical Journal* **44(10)**: 1224–1241.

Lee W, Lee WJ, Lee SB and Salgado R (2004) Measurement of pile load transfer using the fiber bragg grating sensor system. *Canadian Geotechnical Journal* **41(6)**: 1222–1232.

Li GW, Pei HF, Yin JH, Lu XC and Teng J (2014) Monitoring and analysis of phc pipe piles under hydraulic jacking using fbg sensing technology. *Measurement* **49**: 358–367.

Li ZS, Blanc M and Thorel L (2020) Using fibre Bragg grating sensors to estimate the horizontal response of a monopile in geotechnical centrifuge. *International Journal of Physical Modelling in Geotechnics* : 1–25.

Loganathan N, Poulos HG and Stewart DP (2000) Centrifuge model testing of tunnelling-induced ground and pile deformations. *Geotechnique* **50(3)**: 283–294.

MacPherson WN, Silva-Lopez M, Barton JS, Moore A, Jones J, Zhao D, Zhang L, Bennion I, Metje N, Chapman D *et al.* (2006) Tunnel monitoring using multicore fibre displacement sensor. *Measurement Science and Technology* **17(5)**: 1180.

Majumder M, Gangopadhyay TK, Chakraborty AK, Dasgupta K and Bhattacharya D (2008) Fibre bragg gratings in structural health monitoring—present status and applications. *Sensors and Actuators A: Physical* **147(1)**: 150 – 164.

Ng CWW and Lu H (2013) Effects of the construction sequence of twin tunnels at different depths on an existing pile. *Canadian Geotechnical Journal* **51(2)**: 173–183.

Schmidt-Hattenberger C, Straub T, Naumann M, Borm G, Lauerer R, Beck C and Schwarz W (2003) Strain measurements by fiber bragg grating sensors for in situ pile loading tests. In *Smart Structures and Materials 2003: Smart Sensor Technology and Measurement Systems*, vol. 5050, International Society for Optics and Photonics, pp. 289–295.

Song G and Marshall AM (2020a) Centrifuge modelling of tunnelling induced ground displacements: pressure and displacement control tunnels. *Tunnelling and Underground Space Technology* **103**: 103461.

Song G and Marshall AM (2020b) Centrifuge study on the influence of tunnel excavation on piles in sand. *Journal of Geotechnical and Geoenvironmental Engineering* **146(12)**: 04020129.

Song G, Marshall AM and Heron C (2018) A mechanical displacement control model tunnel for simulating eccentric ground loss in the centrifuge. In *9th International Conference of Physical Modelling in Geotechnics: ICPMG*, pp. 455–460.

Stanier SA, Blaber J, Take WA and White D (2015) Improved image-based deformation measurement for geotechnical applications. *Canadian Geotechnical Journal* **53(5)**: 727–739.

Xu J, Franza A and Marshall AM (2020) Centrifuge modelling of tunnel-soil-pile interaction considering the presence of rigid caps. In *4th European Conference of Physical Modelling in Geotechnics: ECPMG*, pp. 1–7.

Ye X, Ni Y and Yin J (2013) Safety monitoring of railway tunnel construction using fbg sensing technology. *Advances in Structural Engineering* **16(8)**: 1401–1409.

Zhang L, Shi B, Zeni L, Minardo A, Zhu H and Jia L (2019) An fiber bragg grating-based monitoring system for slope deformation studies in geotechnical centrifuges. *Sensors* **19(7)**: 1591.

Zhou B, Marshall AM and Yu HS (2014) The effect of relative density on greenfield settlements above tunnels in sands. In *Geoshanghai 2014 - International conference on geotechnical engineering*, ASCE, Shanghai, pp. 96–105.

List of Figures

List of Tables